International Journal of Material Forming (2022) 15: 13
https://doi.org/10.1007/s12289-022-01650-2

ESAFORM 25 YEARS ON

Effect of hydrostatic stress on the strength differential effect in low-carbon steel sheet

Toshihiko Kuwabara[1] · Ren Tachibana[2] · Yusuke Takada[2] · Takayuki Koizumi[3] · Sam Coppieters[4] · Fréderic Barlat[5]

Received: 28 August 2021 / Accepted: 10 January 2022 / Published online: 14 February 2022

Abstract

The effect of hydrostatic stress on the strength differential effect (SDE) in a 0.8-mm-thick low-carbon steel sheet is experimentally investigated. The in-plane compressive stress-strain curve is approximately 10% higher than the uniaxial tensile stress-strain curve at a strain of 0.15, confirming that the test sample exhibited the SDE. A stack compression test in the thickness direction of the test sample is also performed. The measured through-thickness uniaxial compressive stress-strain curve is found to be higher than the equibiaxial tensile stress–thickness plastic strain curves measured using a cruciform equibiaxial tension test (ISO 16842) and a hydraulic bulge test (ISO 16808), indicating a positive correlation between hydrostatic pressure and flow stress. From these experiments, we conclude that the SDE in a low-carbon steel sheet is caused by the effect of hydrostatic pressure on flow stress. However, the pressure coefficient of the test sample, $50-150\ \mathrm{TPa}^{-1}$, is found to be significantly higher than those for high-strength steel alloys and Fe single crystals ($13-23\ \mathrm{TPa}^{-1}$) reported by Richmond and Spitzig (1980).

Keywords Low-carbon steel sheet · Strength differential effect · Stack compression test · In-plane compression test · Equibiaxial tension test · Pressure coefficient

Introduction

The tensile and compressive flow stresses of metallic materials are normally assumed to be identical to each other for a given magnitude of strain. However, some materials exhibit a difference in flow stress between tension and compression. This phenomenon is referred to as the strength differential effect (SDE). In sheet metal forming processes, materials are often subjected to compressive as well as tensile stress states. Therefore, detailed knowledge of the SDE is important for enhancing the accuracy of sheet metal forming simulations.

Richmond and Spitzig [1, 2] demonstrated for both iron-based materials, including Fe single crystals, and 1100 aluminum that the flow stress, σ, exhibits a linear dependence on the hydrostatic pressure p, according to the relation:

$$\sigma = \sigma_0(1 + 3\alpha p) \tag{1}$$

where σ_0 is the flow stress at $p = 0$ and α is a pressure coefficient. Based on the uniaxial tension and compression data from tests performed in a hydrostatic pressure unit, they concluded that α appears to have a constant value (13∼23 TPa^{-1}) for iron-based materials and that it is 56 $\mathrm{TPa}^{-1}$for

This article belongs to the Topical Collection: ESAFORM 25 Years On.

✉ Toshihiko Kuwabara
kuwabara@cc.tuat.ac.jp

1 Division of Advanced Mechanical Systems Engineering, Institute of Engineering, Tokyo University of Agriculture and Technology, 2-24-16 Nakacho, Tokyo 184-8588 Koganei-shi, Japan

2 Department of Mechanical Systems Engineering, Graduate School of Engineering, Tokyo University of Agriculture and Technology, 2-24-16 Nakacho, Koganei-shi, Tokyo 184-8588, Japan

3 Department of Mechanical Engineering, National Institute of Technology, Tokyo College, 1220-2, Kunugida- machi, Hachioji-shi, Tokyo 193-0997, Japan

4 Department of Materials Engineering, KU Leuven, Ghent Technology Campus, Gebroeders De Smetstraat 1, 9000 Ghent, Belgium

5 Graduate Institute of Ferrous and Energy Materials Technology, Pohang University of Science and Technology, 77 Cheongam-ro, Nam-gu, Pohang, Gyeongbuk 37673, Korea

1100 aluminum [2]. They [2] also found that Eq. (1) is quantitatively consistent with a model proposed by Jung [3], who obtained the coefficient α based on the shear stress required to move a screw dislocation and the influence of pressure on the elastic shear modulus. Bulatov et al. (1999) [4] investigated the pressure effect on the glide stress in pure Al using direct atomistic simulations (the molecular statics technique), and suggested that their findings support the conclusion obtained by Spitzig and Richmond [2].

Low-carbon steel sheets, which were not investigated by Richmond and Spitzig [1, 2], also exhibit the SDE. Kuwabara et al. [5] performed an in-plane compression test (IPCT) in the rolling direction (RD) on a 5182-O aluminum alloy sheet and two low-carbon steel sheets using comb-shaped dies. They found that the flow stresses were higher in compression than in tension for the steel sheets, whereas the aluminum alloy sheet did not exhibit the SDE. Shirakami et al. [6] performed IPCTs on a low-carbon steel sheet (SPCE) and 590- and 980-MPa dual phase (DP) steel sheets using comb-shaped dies. They found that SPCE showed the SDE in the diagonal direction (DD) and the transverse direction (TD) but not in the RD. The DP steel sheets exhibited the SDE; the flow stress was consistently higher in compression than in tension for the three directions. Maeda et al. [7] correlated the SDE with the pressure-dependent yield criterion (Eq. (1)) for a DP980 sheet. Moreover, they obtained a pressure coefficient that was consistent with the work of Spitzig and Richmond [1, 2]. Koizumi and Kuroda [8] investigated the SDE in a low-carbon steel sheet for the RD, DD, and TD using a stack compression test (SCT) [9] with compression platens that were coated with polycrystalline diamond (PCD). They found that a 0.2% yield stress and subsequent flow stresses were consistently higher in compression than in tension for the three directions. The magnitude of the SDE in low-carbon steel sheets reported in the above studies is in the range of 0 and 10% of the tensile flow stress and appears to depend on the strain history applied to the specimen. However, no studies have elucidated the cause of the SDE in low-carbon steel sheets. Moreover, the value of α for a low-carbon steel sheet has not been obtained.

The objective of the present study is to experimentally confirm whether the SDE in a low-carbon steel sheet is caused by hydrostatic pressure, as suggested by Richmond and Spitzig [1, 2]. To this end, we compare the results from an SCT in the thickness (normal) direction (ND) with those from a hydraulic bulge test (HBT). Given the identical deformation mode and deviatoric stress state, any discrepancy between the flow stress measured by the SCT and the HBT can be unambiguously attributed to a difference in hydrostatic pressure. This statement is only valid provided that friction can be sufficiently reduced; therefore, we use PCD platens in the SCT, as suggested by Koizumi and Kuroda [8].

The rest of this paper is organized as follows. The next section describes theoretical considerations based on the work of Spitzig and Richmond [1, 2] regarding the role of hydrostatic pressure on flow stress. The experimental methods and results are presented in Sections 3 and 4, respectively. Based on various experiments, the SDE in the low-carbon steel sheet and its dependence on hydrostatic pressure are comprehensively verified in Section. 5. Conclusions are given in Section. 6.

Theory

Pressure coefficient

The Spitzig-Richmond yield condition is given by

$$\bar{\sigma}\left(\boldsymbol{\sigma}\right) = c - \alpha c \mathrm{tr}\boldsymbol{\sigma} = c(1 - \alpha \mathrm{tr}\boldsymbol{\sigma}) \tag{2}$$

where $\boldsymbol{\sigma}$ is the stress tensor, tr $\boldsymbol{\sigma}$ is its trace, $\bar{\sigma}$ is a pressure-independent effective stress, c is a strength parameter, and α is the pressure coefficient. In this study, α measured using tension and compression tests is denoted as α_{uni} and that measured using a HBT and an SCT is denoted as α_{bs}.

For uniaxial tension, $\sigma_{xx} = \sigma_{\mathrm{t}}$ and $\sigma_{pq} = 0$ otherwise. Thus,

$$\bar{\sigma}\left(\boldsymbol{\sigma}\right) = \sigma_{\mathrm{t}} = c\left(1 - \alpha\sigma_{\mathrm{t}}\right) \tag{3}$$

For uniaxial compression, $\sigma_{xx} = -\sigma_{\mathrm{c}}$ and $\sigma_{pq} = 0$ otherwise. Thus,

$$\bar{\sigma}\left(\boldsymbol{\sigma}\right) = \sigma_{\mathrm{c}} = c\left(1 + \alpha\sigma_{\mathrm{c}}\right) \tag{4}$$

Eliminating c from Eqs. (3) and (4) yields

$$\frac{\sigma_{\mathrm{t}}}{\sigma_{\mathrm{c}}} = \frac{1 - \alpha\sigma_{\mathrm{t}}}{1 + \alpha\sigma_{\mathrm{c}}} \tag{5}$$

from which the pressure coefficient determined using the tension and compression tests, α_{uni}, can be extracted as

$$\alpha = \alpha_{\mathrm{uni}} = \frac{\sigma_{\mathrm{c}} - \sigma_{\mathrm{t}}}{2\sigma_{\mathrm{c}}\sigma_{\mathrm{t}}} \tag{6}$$

For the HBT, $\sigma_{xx} = \sigma_{yy} = \sigma_{\mathrm{b}}$ and $\sigma_{pq} = 0$ otherwise. Note that for the pressure-independent quantity, the equivalent stress state is $\sigma_{zz} = -\sigma_{\mathrm{b}}$ and $\sigma_{pq} = 0$ otherwise. Thus,

$$\bar{\sigma}\left(\boldsymbol{\sigma}\right) = \sigma_{\mathrm{b}} = c\left(1 - 2\alpha\sigma_{\mathrm{b}}\right) \tag{7}$$

For the SCT, $\sigma_{zz} = -\sigma_{zc}$ and $\sigma_{pq} = 0$ otherwise. Thus,

$$\bar{\sigma}\left(\boldsymbol{\sigma}\right) = \sigma_{zc} = c\left(1 + \alpha\sigma_{zc}\right) \tag{8}$$

Eliminating c from Eqs. (7) and (8) yields

$$\frac{\sigma_b}{\sigma_{zc}} = \frac{1 - 2\alpha\sigma_b}{1 + \alpha\sigma_{zc}} \tag{9}$$

from which the pressure coefficient determined using the HBT and SCT, α_{bs}, can be extracted as

$$\alpha = \alpha_{bs} = \frac{\sigma_{zc} - \sigma_b}{3\sigma_{zc}\sigma_b} \tag{10}$$

Definition of SDE magnitude

The SDE between tension and compression is defined, independently of the pressure effect, as

$$\beta_{SDE-uni} = 2\frac{\sigma_c - \sigma_t}{\sigma_c + \sigma_t} \tag{11}$$

Similarly, the SDE between in-plane equbiaxial tension (EBT) and through-the-thickness compression is defined as

$$\beta_{SDE-bs} = 2\frac{\sigma_{zc} - \sigma_b}{\sigma_{zc} + \sigma_b} \tag{12}$$

Experimental methods

Test material

The test material used in this study was a 0.8-mm-thick low-carbon steel sheet, SPCD, in JIS G 3141 (The Japan Industrial Standard). Hereafter, the RD, TD, and ND of the material are referred to as the *x*-, *y*-, and *z*-axes, respectively. Table 1 shows the work hardening characteristics and *r*-values of the test sample in the RD, DD, and TD.

Material test methods

All material tests described below were performed with a strain rate of approximately $5 \times 10^{-4}s^{-1}$.

(i) Uniaxial tension test

Uniaxial tensile tests were performed in the RD, DD, and TD using standard tensile specimens [10], whose parallel length and width were 75 and 12.5 mm, respectively. The strain was measured using an extensometer (Shimazu, SSG50-10 H) with a gauge length of 50 mm.

(ii) In-plane compression test

IPCTs were performed in the RD, DD, and TD to evaluate the SDE in the test sample. The measured compressive stress-strain (S-S) curves were also used to validate the SCT (see Sect. 3.2 (v)). Figure 1(a) shows the geometry of the IPCT specimen. Noma and Kuwabara [11] performed a finite element analysis to check the uniformity of the stress distribution in the gauge area of a specimen subjected to in-plane tension–compression. They observed that the stress measurement error was less than 1% when the specimen had the geometry and strain measurement location shown in the figure. The blank holding pressure applied to the specimen was approximately 1% of the 0.2% proof stress of the test sample.

Figure 1(b) and (c) shows the IPCT apparatus used in this study. Figure 1(b) shows an overview of the dies used for applying in-plane compression to a sheet specimen, which is the same as that used in [11, 12]. Figure 1(c) shows an overview of the test apparatus. Lower die 1 is bolted to the lower plate of the die set. Lower die 2 is bolted to the slide rail, so that the die can move in the horizontal direction without friction. A specimen is placed on lower dies 1 and 2 with both ends clamped by clamping jigs (not shown in the figure). Upper dies 1 and 2 are placed on the specimen. The positioning pins (not shown in the figure) fixed to lower dies 1 and 2 align with holes in upper dies 1 and 2. Accordingly, upper die 1 is stationary, and the motion of upper die 2 is synchronized with that of lower die 2. Lower die 2 is connected to a load cell to measure the tension-compression force during a test. It is actuated by hydraulic cylinder A to apply an in-plane tension-compression force to the specimen. Hydraulic cylinder B exerts a blank holding force on the specimen to prevent the buckling of the specimen during a test. The blank holding force is kept constant during a test via a hydraulic control valve. Steel cylindrical rollers are inserted between the blank holding platens and upper dies 1 and 2 so that the blank holding force can

Table 1 Mechanical properties of test material

Tensile Direction /°	$\sigma_{0.2}$ /MPa	r-value	ε_{TS}^{p} *	C** /MPa	n**	ε_0 **
0	142	1.96	0.232	560	0.268	0.0024
45	155	1.73	0.222	566	0.260	0.0031
90	154	2.20	0.232	552	0.265	0.0042

* ε_{TS}^{p} is logarithmic plastic strain giving the maximum tensile load

**Approximated using at $\sigma = C(\varepsilon_0 + \varepsilon^p)^n$ using at $\varepsilon^p = 0.002$ ε_{TS}^{p}

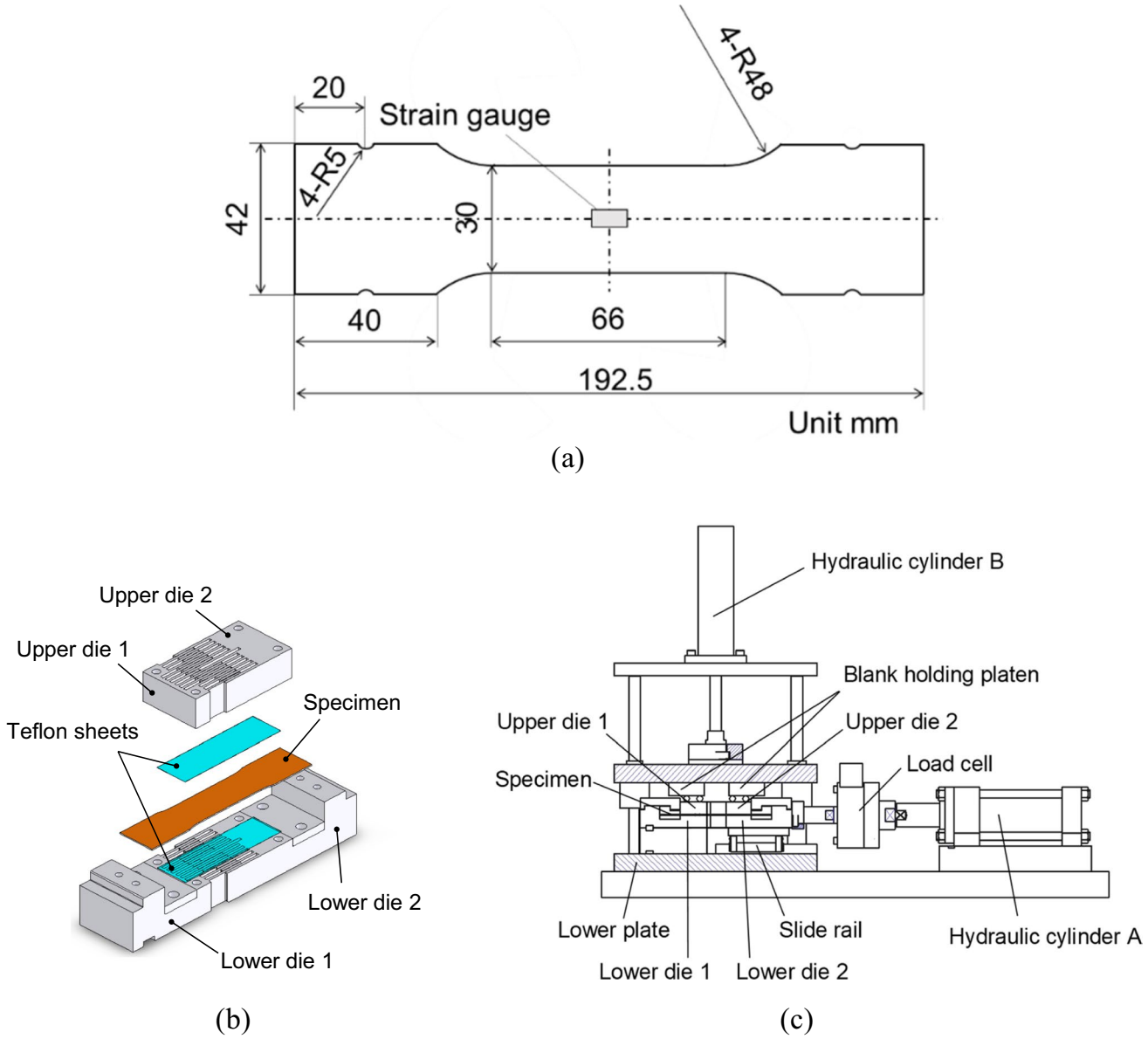

Fig. 1 Experimental apparatus for IPCT: (a) specimen geometry, (b) upper and lower dies, and (c) overview of test apparatus

be transmitted to the specimen during an IPCT without friction.

(iii) Equibiaxial tensile test

An EBT was performed to measure the flow stress at a stress ratio of $\sigma_x : \sigma_y = \sigma_b : \sigma_b = 1 : 1$ using a cruciform specimen, the size and geometry of which are shown in Fig. 2. For details of the test procedures, see ISO 16,842 [13].

(iv) Hydraulic bulge test

The diameter of the die hole was 150 mm and the blank diameter was 220 mm. The $\sigma_b - |\varepsilon_z^p|$ curve was measured using a digital image correlation system. The radius for measuring ε_z^p at the apex was 5.1 mm and that for measuring the radius of curvature was 15 mm.

(v) Uniaxial compression of stacked specimen

The SCT is also referred to as the through-thickness compression test [14], layer compression test [15], or multi-layer upsetting test [16]. The stack can consist of small circular disks [15] or square specimens [14]. Friction between the stack and the compression platens is inevitable. A friction-hill analysis [14] showed that a small height-to-width (or diameter for disks) ratio requires a correction for friction to obtain an accurate

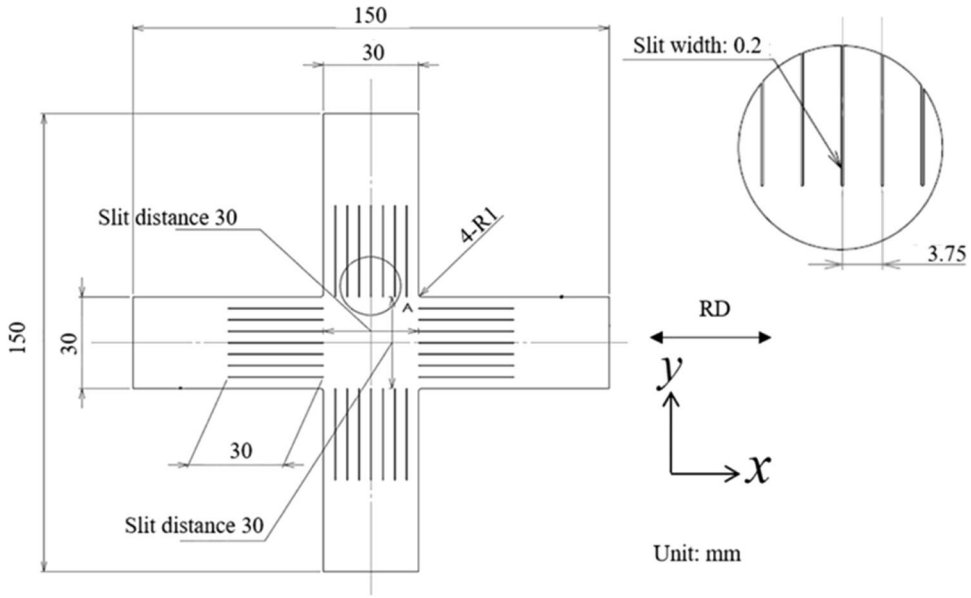

Fig. 2 Specimen geometry for EBT

flow curve. The latter implies that the friction coefficient can be measured, and, more importantly, that it can remain constant during the SCT. The crux of the problem is that the friction condition might vary as lubrication deteriorates due to thinning of the film and extension of the contact surface. Christiansen et al. [17] proposed a mixed experimental-numerical compensation technique to determine the flow curve from upsetting experiments using friction conditions determined through ring compression tests. An and Vegter [14] showed that oiled PFTE film yields constant frictional behavior. Coppieters [18] adopted the modified two specimen method [19] to calibrate the coefficient of friction in the SCT of low-carbon steel and obtained an average value of 0.05. Steglich et al. [20] and Merklein and Godel [15] did not correct for friction when subjecting magnesium alloys and steel sheets to the SCT, respectively. Although correction for friction in the SCT is possible [18], it leads to uncertainty. In the present study, we want to avoid such uncertainty as it potentially biases the uniform stress state in the stack. Consequently, to mitigate the uncertainty related to the frictional condition, the experimental equipment to conduct the SCT was modified in this study.

Figure 3(a) shows a schematic diagram of the uniaxial compression testing device for a stacked specimen. This device was incorporated into a regular tensile testing machine (AUTOGRAPH AG-100kNX, Shimadzu Corporation). Figure 3(b) shows the details of the compression platen. The compression platens have a thickness of 4 mm (a 3-mm-thick super steel base plate coated with 1-mm-thick sintered PCD) and a diameter of 19 mm. PCD reduces the friction between the specimen and the compression platens and thus suppresses the non-uniform deformation of the specimen [8]. The compression platens were positioned on the upper and lower supporting plates using a clamping plate. The supporting plates were bolted to the upper and lower die plates.

Figure 3(c) shows a schematic diagram of the SCT. We performed compression tests using two stacked specimens with the same cross-sectional area but different heights, h_H and h_L, and measured the nominal stress−displacement curve for each specimen. By denoting the difference in displacement between the two stacked specimens for a given nominal stress as Δu and calculating the compressive true strain, ε_z, as $\ln\left(1-\frac{\Delta u}{h_H-h_L}\right)$, we can determine the true stress−true strain curve, $\sigma_{zc}-|\varepsilon_z|$, for a specimen with an initial stack height of $(h_H - h_L)$. This approach enables us to exclude the influences of the elastic deformation of the compression device and potential friction between the specimen and compression platens on the measurement of ε_z. One of the authors previously found that the hydrostatic pressure depends on the stack configuration (i.e., the ratio of the cross-sectional area to the initial height) if friction cannot be avoided [16]. However, this is not a problem in the SCT because friction is minimized by covering the compression platen surfaces with PCD and the change in the aspect ratio of the stack is small.

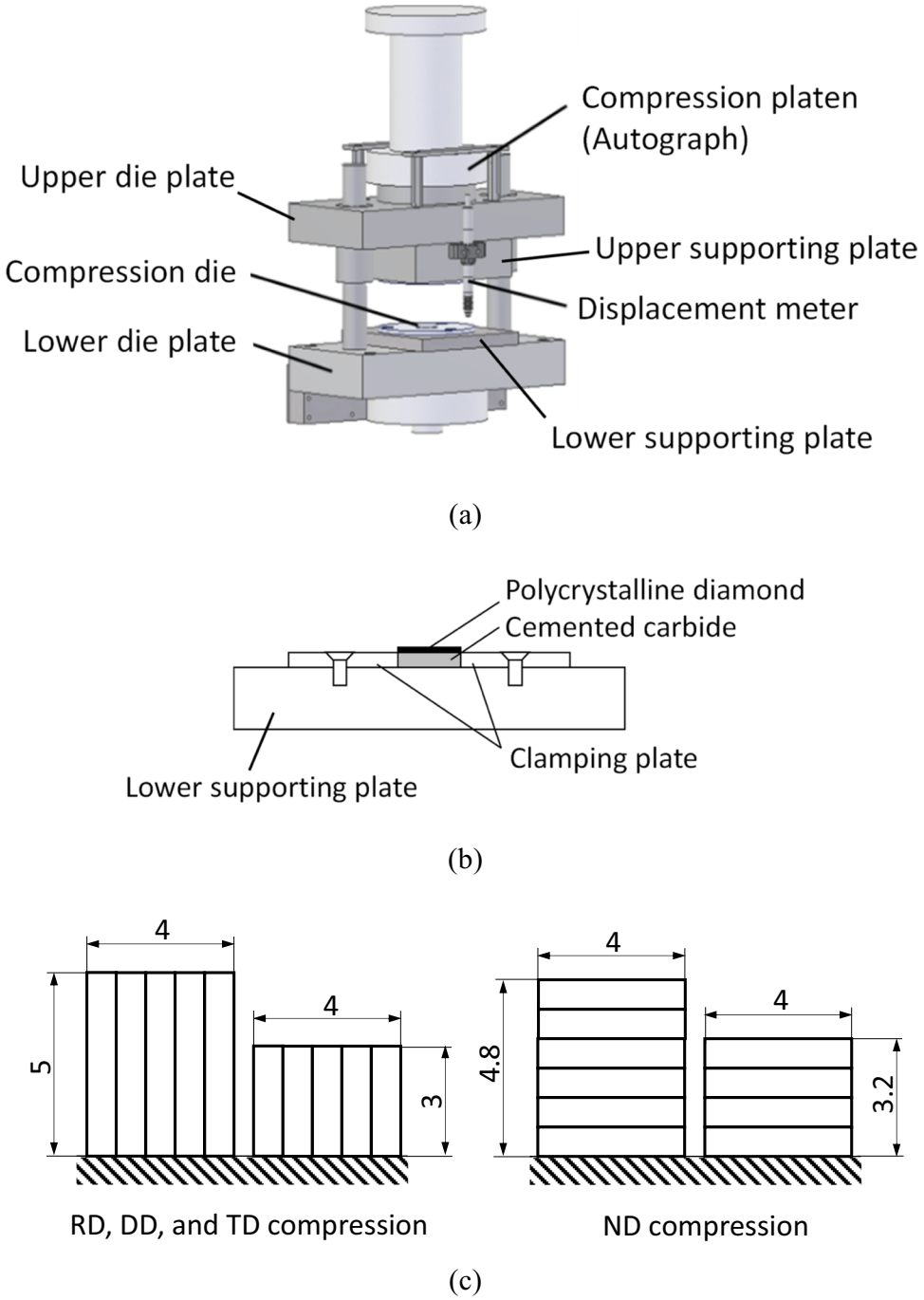

Fig. 3 SCT device: (a) overview of test apparatus, (b) details of lower part of compression die, and (c) specimen geometry

In addition to the ND compression test, SCTs in the RD, DD, and TD of the test sample were performed. The measured compressive S-S curves were compared with those obtained using the IPCT to check the validity of the SCT data. The nominal size of the stacked specimens was 4 mm × 4 mm, parallel to the compression plane, with heights of 5 mm (h_H) and 3 mm (h_L) for the RD, DD, and TD tests (5 sheets were stacked), and 4.8 mm (h_H: 6 sheets were stacked) and 3.2 mm (h_L: 4 sheets were stacked) for the ND test. The stacked specimens were cut to the specified size from a larger stack of glued sheets using a wire electrical discharge machining. The glue used for stacking was CEMEDINE Metal Lock Series Y610 (reactive acrylic adhesive), whose shear strength is 22.8 MPa (http://www.cemedine.co.jp/global/en/technology/sga/metallock/index.html).

Experimental results

SDE in tension and compression

Figure 4 compares the uniaxial tensile true stress–logarithmic plastic strain curves with those measured using the IPCT for the RD, DD, and TD. Each curve shows the average of two specimens. The flow stresses are higher in compression than in tension for all the considered material orientations, showing a clear SDE in the test sample. The $\beta_{\mathrm{SDE-uni}}$ value at a tensile/compressive strain of $|\varepsilon^{\mathrm{p}}| = 0.08$ was 0.071, 0.062, and 0.067 for the RD, DD, and TD, respectively.

Comparison of $\sigma_{\mathrm{b}} - |\varepsilon_z^{\mathrm{p}}|$ curves measured using EBT and HBT

Figure 5 shows the results of the balanced biaxial tension test using two cruciform specimens, Exp. 1 and 2. Figure 5(a) shows the $\sigma_{\mathrm{b}} - \varepsilon_x^{\mathrm{p}}$ and $\sigma_{\mathrm{b}} - \varepsilon_y^{\mathrm{p}}$ curves; the $\sigma_{\mathrm{b}} - \varepsilon_y^{\mathrm{p}}$ curve is slightly higher than the $\sigma_{\mathrm{b}} - \varepsilon_x^{\mathrm{p}}$ curve because of anisotropy. Figure 5(b) shows the $\sigma_{\mathrm{b}} - |\varepsilon_z^{\mathrm{p}}|$ curves. The curves for the two specimens are consistent with each other, confirming reproducibility.

Figure 6 shows the $\sigma_{\mathrm{b}} - |\varepsilon_z^{\mathrm{p}}|$ curves measured using the HBT. In Fig. 6(a), the $\sigma_{\mathrm{b}} - |\varepsilon_z^{\mathrm{p}}|$ curves for specimens Exp. 1 and 2 are shown for a whole strain range; the two curves are consistent with each other. In Fig. 6(b), the average $\sigma_{\mathrm{b}} - |\varepsilon_z^{\mathrm{p}}|$ curve measured using the HBT is compared with that measured using cruciform specimens for a strain range of $0 \le |\varepsilon_z^{\mathrm{p}}| \le 0.10$. The $\sigma_{\mathrm{b}} - |\varepsilon_z^{\mathrm{p}}|$ curves measured using the two test methods are in excellent agreement. The flow stress measured using the HBT is thus valid. The horizontal offset of the HBT flow curve by $|\varepsilon_z^{\mathrm{p}}| \approx 0.006$ is due to the HBT specimen being slightly stretched when clamped to the die.

SCT results

Figure 7(a) and (b) shows the specimens before and after the SCT for the RD and ND of the test sample, respectively. Three specimens, Exp. 1 to 3, were used for each compression direction. The compressive deformation of the stacked specimens is uniform, with no barreling. We also did not observe any barreling for the TD and DD compression.

Figure 8 shows the test results of the SCT in the RD of the test sample. Figure 8(a) shows the load–displacement ($F - u$) curves for displacement ranges of (a-1) $0 \le u \le 0.8$ mm and (a-2) $0 \le u \le 0.10$ mm. Three specimens were used for each SCT, RD-1 and -2, with specimen heights of $h_{\mathrm{L}} = 3$ mm and $h_{\mathrm{H}} = 5$mm, respectively. Good reproducibility of the $F - u$curves was confirmed for both tests. Figure 8(b) shows the $|\sigma_x| - |\varepsilon_x|$ curve measured

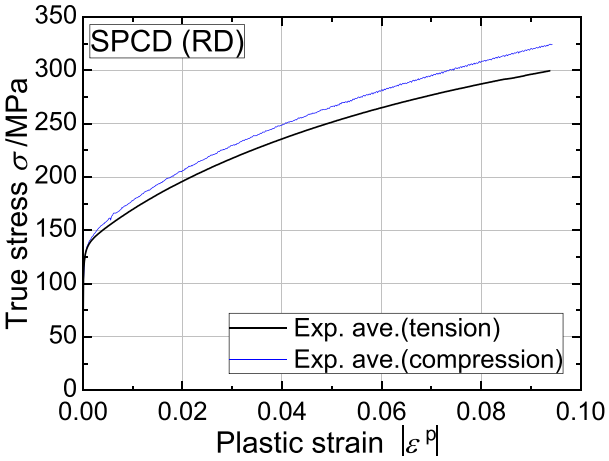

(a) RD

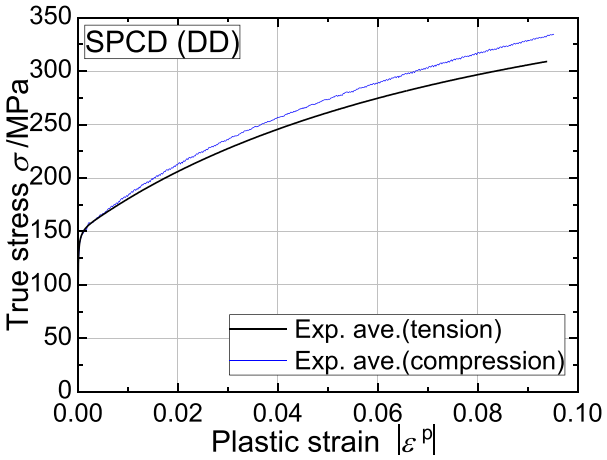

(b) DD

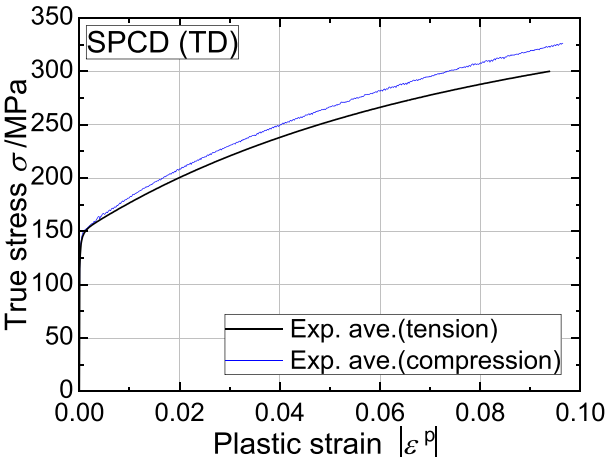

(c) TD

Fig. 4 Comparison of true stress-plastic strain curves between uniaxial tension and in-plane uniaxial compression

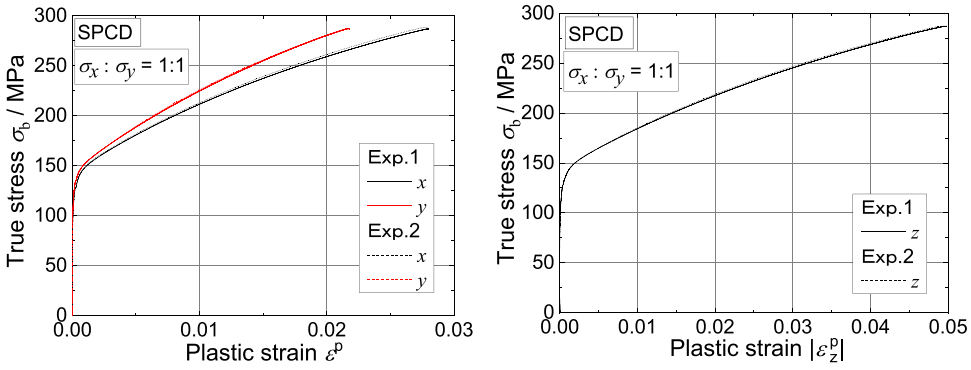

Fig. 5 True stress-logarithmic plastic strain curves for $\sigma_x : \sigma_y = 1 : 1 (\sigma_x = \sigma_y = \sigma_b)$ measured using a cruciform specimen: (a) $\sigma_b - \varepsilon_x^p$ and $\sigma_b - \varepsilon_y^p$ curves; (b) $\sigma_b - \varepsilon_z^p$ curve

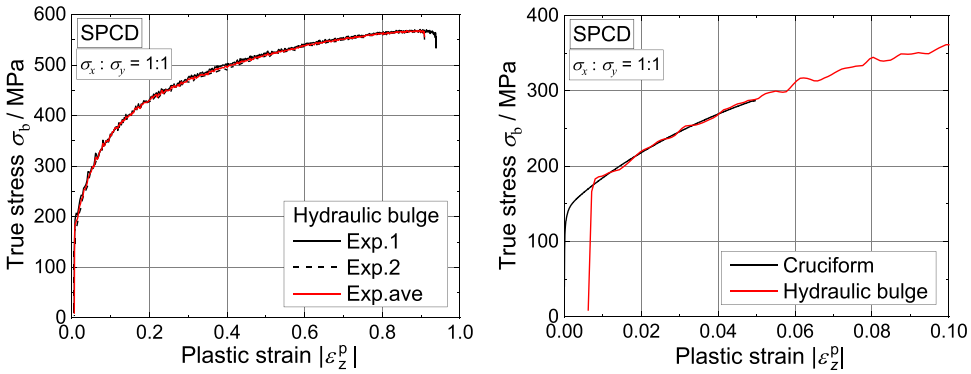

Fig. 6 Test results of HBT: (a) $\sigma_b - \varepsilon_z^p$ curves for whole strain range; (b) enlarged view of $\sigma_b - \varepsilon_z^p$ curves for low strain range of $0 \le \varepsilon_z^p \le 0.10$ with data obtained using cruciform specimen superimposed

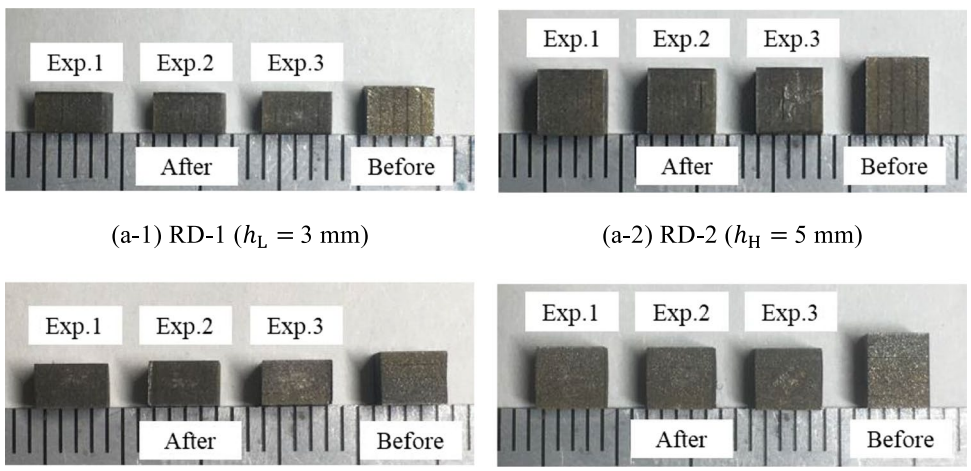

Fig. 7 Specimens before and after SCTs in (a) RD and (b) ND of test sample

using the SCT for strain ranges of (b-1) $0 \le |\varepsilon_x| \le 0.17$ and (b-2) $0 \le |\varepsilon_x| \le 0.04$. The $|\sigma_x| - |\varepsilon_x|$ curve obtained by subtracting the displacement of RD-1 from that of RD-2 for a given nominal stress is consistent with that measured using the IPCT with a single test piece (see Fig. 1(a)). This confirms the validity of the SCT. The validity of the DD and TD compression test results was also confirmed.

Figure 9 shows the test results of the SCT in the ND of the test sample. Figure 9(a) shows the $F - u$ curves for displacement ranges of (a-1) $0 \le u \le 0.9$ mm and (a-2) $0 \le u \le 0.10$ mm. Three specimens were used for each

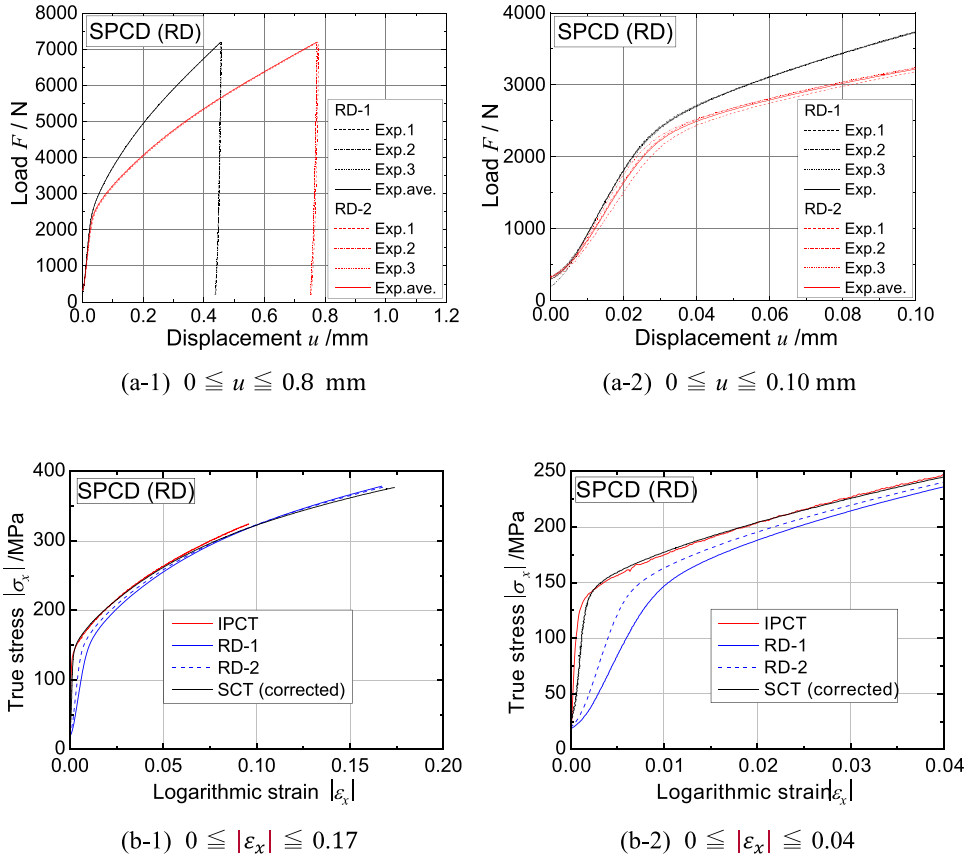

Fig. 8 Results of SCTs in RD of test sample: (a) load-displacement ($F-u$) curves for displacement ranges of (a-1) $0 \leqq u \leqq 0.8$ mm and (a-2) $0 \leqq u \leqq 0.10$ mm; (b) $|\sigma_x| - |\varepsilon_x|$ curves measured using SCT for strain ranges of (b-1) $0 \leqq |\varepsilon_x| \leqq 0.17$ and (b-2) $0 \leqq |\varepsilon_x| \leqq 0.04$. In (b-1) and (b-2), $|\sigma_x| - |\varepsilon_x|$ curve measured using IPCT (Fig. 1) is superimposed

SCT, ND-1 and -2, with specimen heights of $h_L = 3.2$ mm and $h_H = 4.8$mm, respectively. Good reproducibility of the $F-u$curves was confirmed for both tests. Figure 9(b) shows the $|\sigma_z| - |\varepsilon_z|$ curves measured using the SCT for strain ranges of (b-1) $0 \leqq |\varepsilon_z| \leqq 0.20$ and (b-2) $0 \leqq |\varepsilon_x| \leqq 0.04$. In Fig. 9(b), the initial slope of the S-S curve was 26 GPa with loading. 209 GPa was measured for the unloading S-S curve following compression to a strain of -0.2. The initial slope of the S-S curve was much smaller than the original Young's modulus because the upper and lower surfaces of the specimen were not perfectly parallel to each other and the surface roughness of the sheet sample absorbed some of the compressive deformation until the surfaces completely conformed to the compression tool surfaces. Only a few local asperities initially establish contact with the tools. The local pressure then becomes sufficiently high to plastically deform the asperities until full contact with the surfaces is established. This phenomenon lowers the apparent stiffness of the stack. Finally, the adhesively bonded interface between adjacent specimens has a finite thickness, which may affect the overall stiffness of the stack.

Figure 10 compares the S-S curves measured using the uniaxial tension test, IPCT, and SCT in the RD, DD, and TD. The S-S curves obtained from the IPCTs are consistent with those obtained from the SCTs. Moreover, the compressive flow stresses are clearly higher than the tensile flow stresses in all three directions; this confirms the SDE in the test sample.

Figure 11 compares the $\sigma_b - |\varepsilon_z^p|$ curve measured using the EBT and HBT with the $|\sigma_{zc}| - |\varepsilon_z^p|$ curves measured using the SCT in the ND. For the SCT, $|\varepsilon_z^p|$ was obtained by subtracting the elastic strain from the measured total strain, in which the Young's modulus was assumed to be 26 or 209 GPa; the former was measured for the initial elastic loading and the latter was measured from the unloading S-S curve following compression to a strain of -0.2. Both $|\sigma_{zc}| - |\varepsilon_z^p|$ curves are clearly higher than the $\sigma_b - |\varepsilon_z^p|$ curve; the real $|\sigma_{zc}| - |\varepsilon_z^p|$ curve of the test sample should be between the two $|\sigma_{zc}| - |\varepsilon_z^p|$ curves. Thus, our results confirm that the equibiaxial flow stress increases when the hydrostatic stress component increases. This is consistent with the SDE shown in Fig. 10, where a higher hydrostatic stress leads to higher flow stress. A discrepancy between the SCT and the HBT was previously reported by Coppieters et al. [21] and Coppieters et al. [18] for a low-carbon steel sheet and a DP600 steel sheet, respectively. In contrast, Merklein and Godel [15] found good agreement between the SCT and the HBT for DC04 and DX56 steel sheets. Mulder et al. [22] found a discrepancy between the SCT and the HBT for DC06. According to Mulder et al. [23], however, the discrepancy

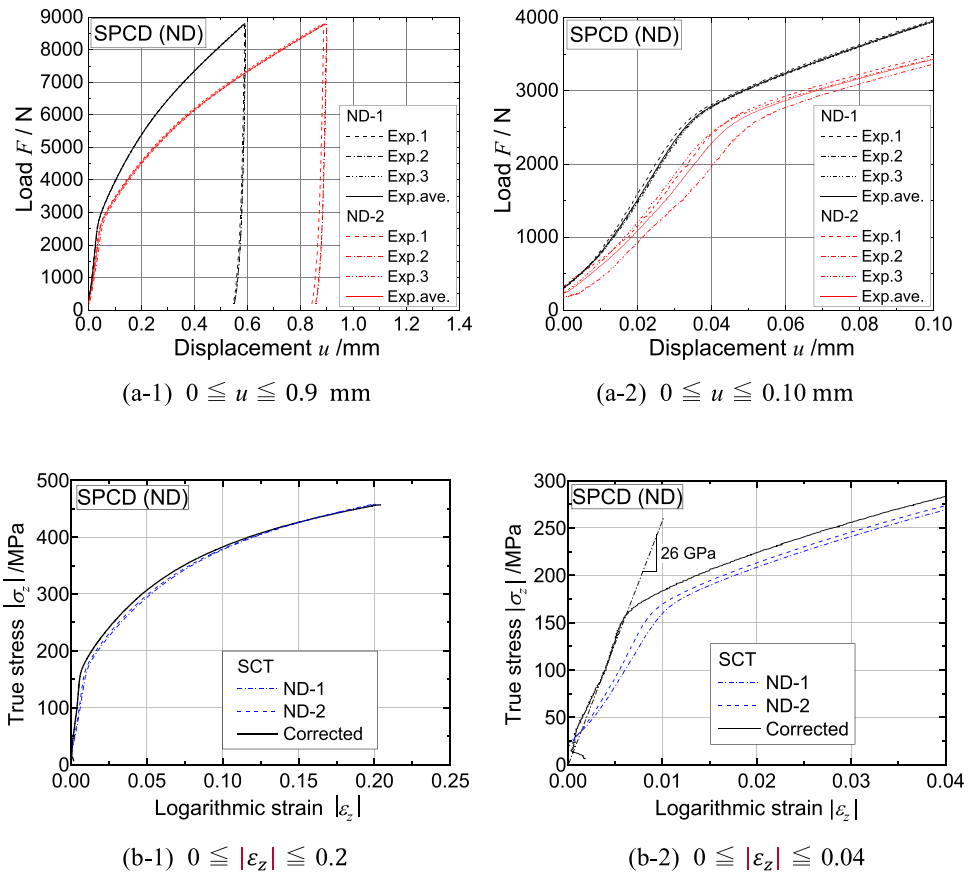

Fig. 9 Results of SCTs in ND of test sample: (**a**) Load-displacement ($F-u$) curves for displacement ranges of (a-1) $0 \leqq u \leqq 0.9$ mm and (a-2) $0 \leqq u \leqq 0.10$ mm; (**b**) $|\sigma_z| - |\varepsilon_z|$ curves measured using SCT for strain ranges of (b-1) $0 \leqq |\varepsilon_z| \leqq 0.20$ and (b-2) $0 \leqq |\varepsilon_z| \leqq 0.04$

could be attributed to different test conditions (i.e., strain rate and temperature effects). Given that we carefully controlled the test conditions and mitigated the frictional effects in this study, the results presented here are deemed trustworthy.

Discussion

Figure 12(a) shows the variation of $\beta_{\mathrm{SDE-uni}}$, as defined in Eq. (11), with increasing plastic strain, $|\varepsilon^{\mathrm{p}}|$. The data of $\beta_{\mathrm{SDE-uni}}$ are shown for $|\varepsilon^{\mathrm{p}}| \geq 0.005$ because the SCT data for $|\varepsilon^{\mathrm{p}}| < 0.005$ were not reliable. In the strain range of $0.005 < |\varepsilon^{\mathrm{p}}| < 0.16$, the measured $\beta_{\mathrm{SDE-uni}}$ in this study, i.e., $0.02 < \beta_{\mathrm{SDE-uni}} < 0.10$, is consistent with previous findings by one of the present authors [5] and Koizumi and Kuroda [8] for low-carbon steel sheets. However, Koizumi and Kuroda's results [8] showed an almost constant $\beta_{\mathrm{SDE-uni}}$ ($0.06 \leq \beta_{\mathrm{SDE-uni}} \leq 0.07$) for the TD and DD in the strain range of $0.01 \leq \varepsilon^{\mathrm{p}} \leq 0.04$ followed by a monotonic increase of $\beta_{\mathrm{SDE-uni}}$ for $\varepsilon^{\mathrm{p}} \geq 0.04$ (see Fig. 12(b)). The $\beta_{\mathrm{SDE-uni}}$ in this study, in contrast, monotonically increases in the strain range of $0.01 \leq \varepsilon^{\mathrm{p}}$ in the TD and DD (see Fig. 12(a)). Therefore, the magnitude of the SDE observed in Fig. 12 (or Fig. 10) is considered to be a common characteristic of a group of low-carbon steel sheets.

Figure 13 shows the variation of $\beta_{\mathrm{SDE-bs}}$, as defined in Eq. (12), with increasing thickness plastic strain, $|\varepsilon_z^{\mathrm{p}}|$. The data of $\beta_{\mathrm{SDE-bs}}$, for which the Young's modulus of the stacked specimen is assumed to be 209 GPa, are shown only for $|\varepsilon_z^{\mathrm{p}}| \geq 0.008$ because the SCT data in the ND for $|\varepsilon_z^{\mathrm{p}}| < 0.008$ were not reliable, as shown in Fig. 9(b-2). $\beta_{\mathrm{SDE-bs}}$ values of $0.075 < \beta_{\mathrm{SDE-bs}} < 0.20$ and $0 < \beta_{\mathrm{SDE-bs}} < 0.08$ were obtained for 26 and 209 GPa as the assumed Young's modulus of the stacked specimen, respectively. The actual $\beta_{\mathrm{SDE-bs}}$ should be within these ranges; it appears to converge to approximately 0.06 to 0.07 for a strain range of $|\varepsilon_z^{\mathrm{p}}| > 0.15$. $\beta_{\mathrm{SDE-bs}}$ is affected by the magnitude of the offset of the $|\sigma_{zc}| - |\varepsilon_z^{\mathrm{p}}|$ curves in Fig. 11, or, equivalently, by the assumed value of Young's modulus. Therefore, we can safely conclude that $\beta_{\mathrm{SDE-bs}}$ can be estimated to be between 0.05 and 0.10 for a strain range of $|\varepsilon_z^{\mathrm{p}}| > 0.10$.

From Figs. 12 and 13, we conclude that the uniaxial compressive flow stresses in the RD, DD, and TD are larger than the tensile ones, and that the uniaxial compressive flow stress in the ND is larger than the equibiaxial tensile flow stress. Therefore, we experimentally confirmed that the SDE in the low-carbon steel sheet is caused by the effect of hydrostatic pressure on flow stress.

Figure 14 shows the development of α_{uni} with $|\varepsilon^{\mathrm{p}}|$ calculated using Eq. (6) for the SCT and the IPCT.

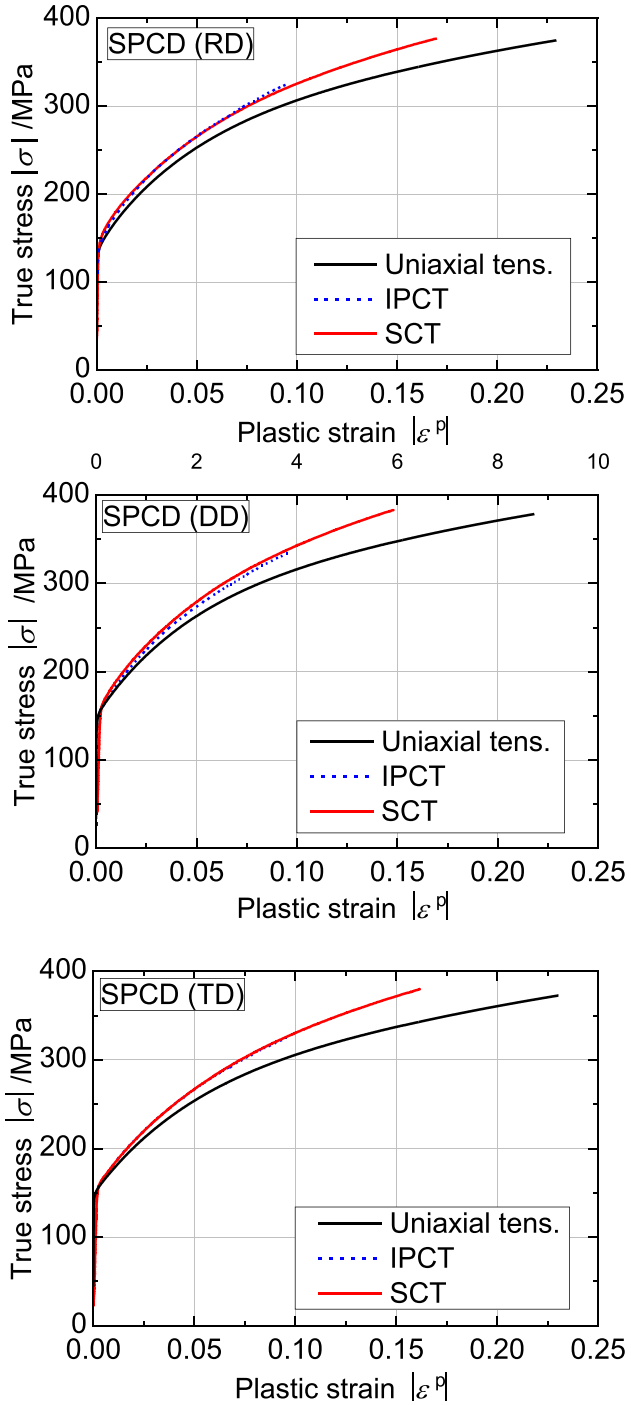

Fig. 10 Comparison of true stress-plastic strain curves between uniaxial tension, in-plane compression, and stacked compression in RD, DD, and TD

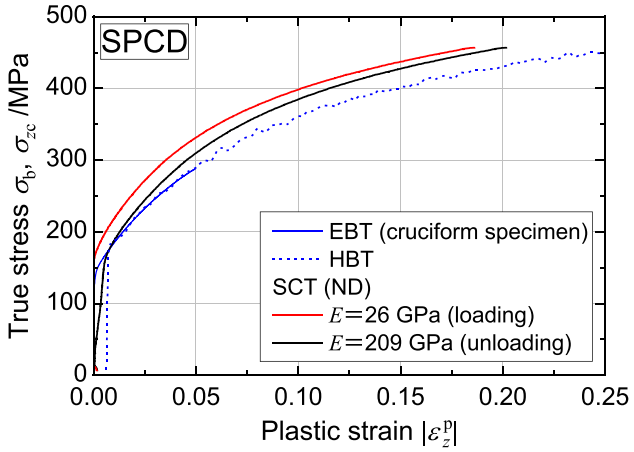

Fig. 11 Comparison of true stress-plastic strain curve for HBT, cruciform biaxial tension test, and SCT

The α_{uni} measured using the SCT is not shown for $|\varepsilon^p| < 0.005$ because the data were not reliable for this strain range. For the present test sample, the α_{uni} takes values of $50 < \alpha_{uni} < 150\ \mathrm{TPa}^{-1}$ for a strain range of $0.02 < |\varepsilon^p| < 0.16$. It is noteworthy that the values measured using the IPCT rapidly increase during the initial strain range. This is consistent with the behavior of Fe single crystals observed by Spitzig [24], who claimed that the increase in the initial work-hardening rate under pressure can be rationalized on the basis of reduced dislocation generation under pressure because of the increase in volume associated with an increase in dislocation density.

Figure 15 shows the development of α_{bs} with $|\varepsilon_z^p|$ calculated by substituting the data of the HBT and the SCT in the ND into Eq. (10). The data of α_{bs}, for which the Young's modulus of the stacked specimen is assumed to be 209 GPa, are shown only for $|\varepsilon_z^p| \geq 0.008$ because the SCT data in the ND for $|\varepsilon_z^p| < 0.008$ were not reliable. α_{bs} values of $50 \leq \alpha_{bs} \leq 350\ \mathrm{TPa}^{-1}$ and $0 < \alpha_{bs} < 100\ \mathrm{TPa}^{-1}$ were obtained for 26 and 209 GPa as the assumed Young's modulus of the stacked specimen, respectively. The actual α_{bs} should be within these ranges; it appears to converge to approximately 50 to 60 $\mathrm{TPa}^{-1}$for a strain range of $|\varepsilon_z^p| > 0.15$. α_{bs} is affected by the magnitude of the offset of the $|\sigma_{zc}| - |\varepsilon_z^p|$ curves in Fig. 11, or, equivalently, the assumed value of Young's modulus. Therefore, if we take the average of the α_{bs} of the two curves, we can conclude that α_{bs} can be estimated to gradually decrease from 150 to 50 TPa^{-1} as $|\varepsilon_z^p|$ increases from 0.02 to 0.18.

The values of α_{uni} and α_{bs} obtained in this study are two to seven times larger than those reported by Richmond and Spitzig [1, 2], $13 < \alpha_{uni} < 23\ \mathrm{TPa}^{-1}$, for iron-based materials, including Fe single crystals. Moreover, these authors showed that α_{uni} is constant for a strain range of 0 to 0.04 for 4330 steel and 0 to 0.02 for aged maraging steel [1]. Therefore, our experimental results, which showed that the test sample's α_{uni} is $(50 - 150)\ \mathrm{TPa}^{-1}$ for $|\varepsilon^p| > 0.02$ and that α_{bs} gradually decreases from 150 to 50 TPa^{-1} as $|\varepsilon_z^p|$ increases from 0.02 to 0.18, are novel. The present authors do not consider the magnitudes of α_{uni} and α_{bs} of the test sample to

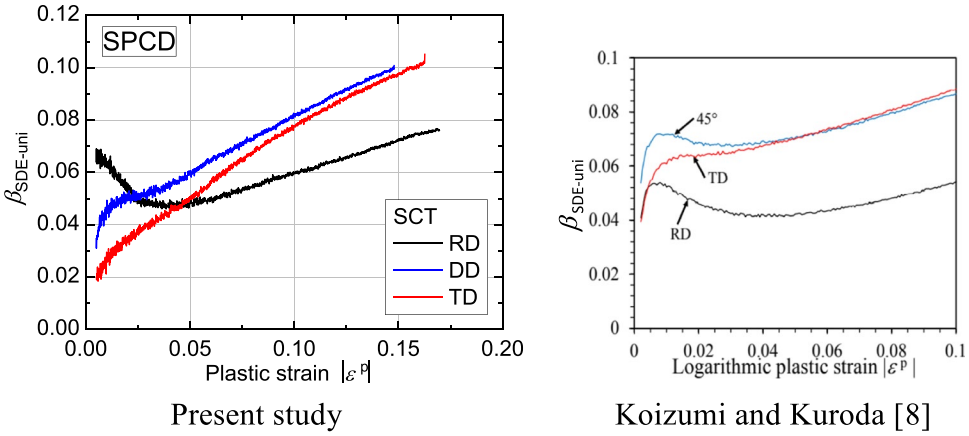

Fig. 12 $\beta_{SDE\text{-}uni} - |\varepsilon^p|$ curves for RD, DD, and TD calculated using Eq. (11)

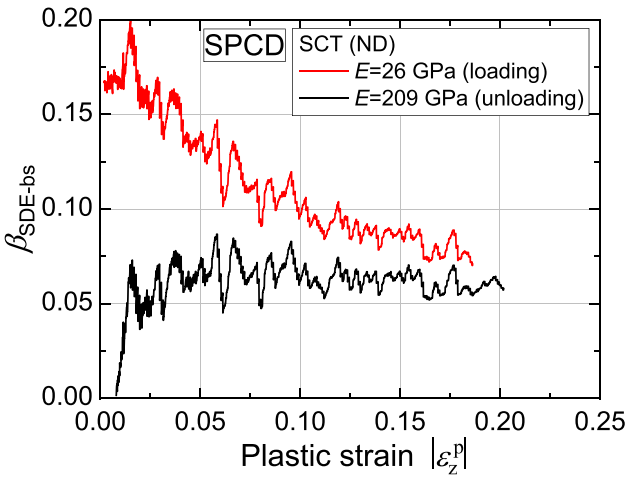

Fig. 13 $\beta_{SDE-bs} - |\varepsilon_z^p|$ curves calculated using Eq. (12)

be a universal property of low-carbon steel sheets. Shirakami et al. [6] found that in a low-carbon steel sheet, the SDE was strong in the DD and TD but weak in the RD. The difference in the degree of the SDE in low-carbon steel sheets between various studies may be caused by differences in the strain history applied to the test materials during the manufacturing process. Further studies are required.

Regarding the reason why the value of α of the test sample is higher than those reported by Richmond and Spitzig [1, 2], there is a possibility that the tension-compression asymmetry may also depend on a mechanism unrelated to pressure. Gröger et al. [25, 26] investigated the atomistic and continuum modeling of molybdenum and tungsten, two body-centered cubic (bcc) materials (iron is also bcc). They found that for tensile/compressive loading, the Schmid law breaks down in bcc metals; the critical resolved shear stress in the slip direction depends sensitively on the shear stress perpendicular to the slip direction because it alters the dislocation core. As a result, the critical resolved shear stress in tension is always lower than in compression. Therefore, we conclude that the experimental results obtained in our study do not contradict the observation that hydrostatic stress influences the SDE. However, the strong SDE observed suggests that another mechanism, which has been observed and justified in single-phase bcc metals [25, 26], also contributes.

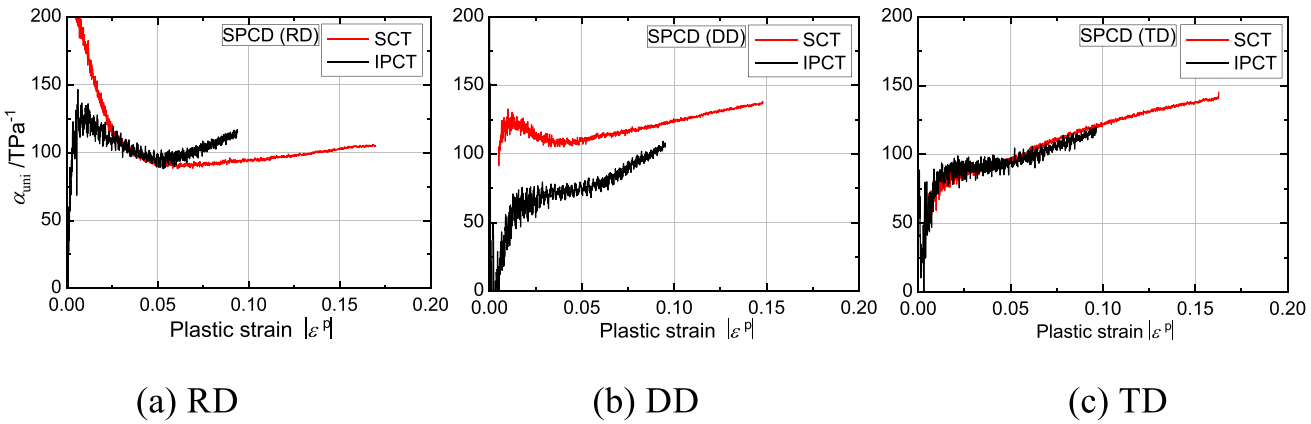

Fig. 14 $\alpha_{uni} - |\varepsilon^p|$ curves calculated using Eq. (6) with data from SCT and IPCT

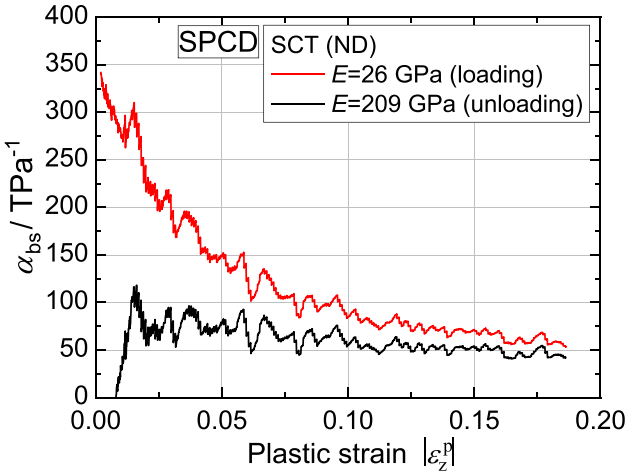

Fig. 15 $\alpha_{bs} - |\varepsilon_z^p| + |\varepsilon_z^p|$ curves calculated using Eq. (10)

It is well known that ductile polymers (e.g. thermoplastics) subjected to cold forming exhibit the SDE and that it affects the material behavior and formability [27, 28]. The experimental technique developed in this study (Fig. 3) would be useful for accurately identifying the SDE of ductile polymers.

Conclusions

The uniaxial flow stress of a low-carbon steel sheet with an average *r*-value of 1.91 was higher in compression than in tension, indicating the presence of the SDE. To determine whether the SDE was caused by the hydrostatic stress component, as suggested by Richmond and Spitzig [1, 2] for high-strength steel alloys and Fe single crystals, the equibiaxial flow stress of the test sample was also measured using the HBT and EBT, and was compared with the uniaxial compressive flow stress in the ND measured using the SCT. We found that the latter is larger than the former. Therefore, we conclude that the SDE in the test sample is possibly caused by the effect of hydrostatic pressure on flow stress. However, the pressure coefficient of the test sample, $\alpha_{uni}, \alpha_{bs} \approx (50 - 150)$ TPa^{-1} for $|\varepsilon^p| > 0.02$, became significantly higher than those reported by Richmond and Spitzig [1, 2], $13 < \alpha_{uni} < 23$ TPa^{-1}, for iron-based materials, including Fe single crystals.

The discrepancy in the value of the pressure coefficient α between the present experiment and those of Richmond and Spitzig [1, 2] might be explained by a mechanism unrelated to pressure that contributes to the SDE. This mechanism could be related to the dislocation core structure in bcc metals, as suggested by Gröger et al. [25, 26]. Although Spitzig measured the pressure coefficient in Fe single crystals, he did not measure the SDE [24]. Therefore, the origin of the SDE in low-carbon steel sheets requires further study.

Authors' contributions All authors contributed to the study conception and design. Material preparation, data collection and analysis were performed by Toshihiko Kuwabara, Ren Tachibana, and Yusuke Takada. The first draft of the manuscript was written by Toshihiko Kuwabara and Ren Tachibana and all authors commented on previous versions of the manuscript. All authors read and approved the final manuscript.

Declarations

Conflicts of interest/Competing interests The authors have no relevant financial or non-financial interests to disclose.

References

1. Richmond O, Spitzig WA (1980) Pressure dependence and dilatancy of plastic flow. IUTAM Conference, Theoretical and Applied Mechanics, Proc. 15th International Congress of Theoretical and Applied Mechanics. North-Holland Publishers, Amsterdam, pp 377–386
2. Spitzig WA, Richmond O (1984) The effect of pressure on the flow stress of metals. Acta Metall 32:457–463. https://doi.org/10.1016/0001-6160(84)90119-6
3. Jung J (1981) A note on the influence of hydrostatic pressure on dislocations. Philos Mag A 43:1057–1061. https://doi.org/10.1080/01418618108239511
4. Bulatov VV, Richmond O, Glazov MV (1999) An atomistic dislocation mechanism of pressure-dependent plastic flow in aluminum. Acta Mater 47:3507–3514. https://doi.org/10.1016/S1359-6454(99)00154-8
5. Kuwabara T, Morita Y, Miyashita Y, Takahashi S (1995) Elastic-Plastic Behavior of Sheet Metal Subjected to In-Plane Reverse Loading. Proc. Plasticity '95, The fifth international symposium on plasticity and its current applications, ed. S Tanimura S, Khan AS. Gordon and Breach Publishers, London, pp 841-844
6. Shirakami S, Kuwabara T, Tsuru E (2017) Axial compressive deformation behavior and material modeling of steel pipe with bending deformation history. J JSTP 58:692–698 (in Japanese). https://doi.org/10.9773/sosei.58.692
7. Maeda T, Noma N, Kuwabara T, Barlat F, Korkolis YP (2018) Measurement of the strength differential effect of DP980 steel sheet and experimental validation using pure bending test. J Mater Process Technol 265:247–253. https://doi.org/10.1016/j.jmatprotec.2018.02.009
8. Koizumi T, Kuroda M (2018) Evaluation of tension-compression asymmetry of a low-carbon steel sheet using a modified classical compression test method. IOP Conf. Series, J Phys 1063
9. Alves LM, Nielsen CV, Martins PAF (2011) Revisiting the fundamentals and capabilities of the stack compression test. Exp Mech 51:1565–1572. https://doi.org/10.1007/s11340-011-9480-5
10. ISO 6892-1: 2019 Metallic materials — Tensile testing — Part 1:Method of test at room temperature
11. Noma N, Kuwabara T (2012) Numerical investigation of specimen geometry for in-plane compression tests and its experimental validation. J JSTP 53:574–578 (in Japanese). https://doi.org/10.9773/sosei.53.574
12. Kuwabara T, Kumano Y, Ziegelheim J, Kurosaki I (2009) Tension-compression asymmetry of phosphor bronze for electronic

parts and its effect on bending behavior. Int J Plast 25:1759–1776. https://doi.org/10.1016/j.ijplas.2009.01.004
13. ISO 16842: 2021 Metallic materials –Sheet and strip – Biaxial tensile testing method using a cruciform test piece
14. An YG, Vegter H (2005) Analytical and experimental study of frictional behavior in through-thickness compression test. J Mat Proc Technol 160:148–155. https://doi.org/10.1016/j.jmatprotec.2004.05.026
15. Merklein M, Godel V (2009) Characterization of the flow behavior of deep drawing steel grades in dependency of the stress state and its impact on FEA. Int J Mater Forming 2:415–418. https://doi.org/10.1007/s12289-009-0506-9
16. Jäckel M, Drossel W-G, Vandermeiren N, Maas F, Coppieters S, Debruyne D (2020) Standardization of flow curve determination for joining by forming, EFB-Forschungsbericht Nr.534. https://www.efb.de/efb-forschungsbericht-nr-534.html-1602681469.html
17. Christiansen P, Martins PAF, Bay N (2016) Friction compensation in the upsetting of cylindrical test specimens. Exp Mech 56 (2016):1271–1279. https://doi.org/10.1007/s11340-016-0164-z
18. Coppieters S, Jäckel M, Kraus C, Kuwabara T, Barlat F (2020) Influence of a hydrostatic pressure shift on the flow stress in sheet metal. Procedia Manuf 47:1245–1249. https://doi.org/10.1016/j.promfg.2020.04.196
19. Han H (2002) The validity of mechanical models evaluated by two-specimen method under the unknown coefficient of friction and flow stress. J Mater Process Technol 122:386–396. https://doi.org/10.1016/S0924-0136(02)00059-6
20. Steglich D, Tian X, Bohlen J, Kuwabara T (2014) Mechanical testing of thin sheet magnesium alloys in biaxial tension and uniaxial compression. Exp Mech 54:1447–1258. https://doi.org/10.1007/s11340-014-9892-0
21. Coppieters S, Jäckel M, Miyake N, Kraus C, Traphoner H, Kuwabara T, Tekkaya EA (2019) Large strain flow curve identification for sheet metal: process-informed method selection. Forming Technology Forum 2019. 19-20 September 2019, Herrsching/Ammersee, Germany
22. Mulder J, Vegter H, Ha JJ, van den Boogaard AH (2012) Determination of flow curves under equibiaxial stress conditions. Key Eng Mater 504–506:53–58
23. Mulder J, Vegter H, van den Boogaard AH (2015) An engineering approach to strain rate and temperature compensation of the flow stress established by the hydraulic bulge test. Key Eng Mater 651–653:138–143. https://doi.org/10.4028/www.scientific.net/KEM.651-653.138
24. Spitzig WA (1979) Effect of hydrostatic pressure on plastic-flow properties of iron single crystals. Acta Metall 27:523–534. https://doi.org/10.1016/0001-6160(79)90004-X
25. Gröger R, Bailey AG, Vitek V (2008) A Multiscale modeling of plastic deformation of molybdenum and tungsten: II. tomistic studies of the core structure and glide of 1/2<111> screw dislocations at 0 K. Acta Mat 56: 5401-5411. https://doi.org/10.1016/j.actamat.2008.07.018
26. Gröger R, Racherla V, Bassani JL, Vitek V (2008) Multiscale modeling of plastic deformation of molybdenum and tungsten: II. Yield criterion for single crystals based on atomistic studies of glide of 1/2<111> screw dislocations. Acta Mat 56: 5412-5425. https://doi.org/10.1016/j.actamat.2008.07.037
27. Spitzig WA and Richmond O (1979) Effect of Hydrostatic pressure on the deformation behavior of polyethylene and polycarbonate in tension and in compression. Polymer Engng Sci 19: 1129. https://doi.org/10.1002/pen.760191602
28. Nielsen CV and Martins PAF (2021) Metal forming: formability, simulation, and tool design. Academic, Cambridge, pp 231-233